ACS NANO

www.acsnano.org

ARTICLE

Transforming Detrimental Crystalline Zinc Hydroxide Sulfate to Homogeneous Fluorinated Amorphous Solid–Electrolyte Interphase on Zinc Anode

Siyu Tian,[#] Taesoon Hwang,[#] Zhuoxun Zhang, Shiwen Wu, Amirarsalan Mashhadian, Renzheng Zhang, Tye Milazzo, Tengfei Luo, Ruda Jian, Tianyi Li, Kyeongjae Cho,* and Guoping Xiong*

Cite This: *ACS Nano* 2025, 19, 3135–3146

Read Online

ACCESS | Metrics & More | Article Recommendations | Supporting Information

ABSTRACT: The formation of non-ion conducting byproducts on zinc anode is notoriously detrimental to aqueous zinc-ion batteries (AZIBs). Herein, we successfully transform a representative detrimental byproduct, crystalline zinc hydroxide sulfate (ZHS) to fast-ion conducting solid-electrolyte interphase (SEI) via amorphization and fluorination induced by suspending CaF_2 nanoparticles in dilute sulfate electrolytes. Distinct from widely reported nonhomogeneous organic–inorganic hybrid SEIs that exhibit structural and chemical instability, the designed single-phase SEI is homogeneous, mechanically robust, and chemically stable. These characteristics of the SEI facilitate the prevention of zinc dendrite growth and reduction of capacity loss during long-term cycling. Importantly, AZIB full cells based on this SEI-forming electrolyte exhibit exceptional stability over 20,000 cycles at 3 A/g with a charging voltage of 2.2 V without short circuits and electrolyte dry-out. This work suggests avenues for designing SEIs on a metal anode and provides insights into associated SEI chemistry.

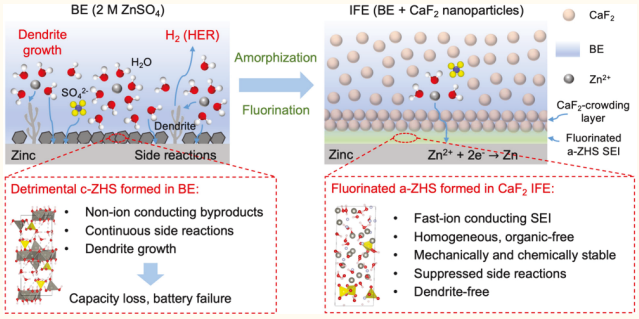

KEYWORDS: *Electrolyte, Solid-electrolyte interphase, Zinc hydroxide sulfate, Fluorination, Amorphization, Zinc anode*

1. INTRODUCTION

Aqueous zinc-ion batteries (AZIBs) based on zinc anode and mild acidic electrolytes are promising for large-scale energy storage due to their advantages, including high safety, low cost, and environmental friendliness.[1,2] They demonstrate excellent sustainability, given the high abundance and low cost of zinc and associated cathode materials (e.g., V_2O_5, MnO_2). Zinc anode also possesses a high theoretic capacity of 820 mAh/g and an appropriate redox potential of −0.76 V vs the standard hydrogen electrode.[3] However, the development of AZIBs faces critical challenges due to spontaneous hydrogen evolution reaction (HER) and HER-triggered byproduct formation. For instance, in conventional sulfate electrolytes, highly crystallized zinc hydroxide sulfate (c-ZHS), $Zn_4(OH)_6SO_4{\cdot}xH_2O$, is spontaneously formed on zinc anode via the following reactions:[4]

$$2H_2O + 2e^- \rightarrow 2OH^- + H_2 \quad (1)$$

$$4Zn^{2+} + 6OH^- + SO_4^{2-} + xH_2O \rightarrow Zn_4(OH)_6SO_4{\cdot}xH_2O\ (\text{crystalline}) \quad (2)$$

Similar side reactions and crystalline ZHS-analogues have been observed ubiquitously for the zinc anode paired with mild acidic electrolytes, such as zinc acetate, zinc triflate, zinc chloride, and zinc nitrite.[5,6] These non-ion conducting byproducts have been known to block Zn^{2+} diffusion pathways and promote zinc dendrite growth between ZHS-covered zinc anode surfaces, making them detrimental passivation layers on zinc anode that only accelerate capacity loss and battery failure.[5,6]

Received: April 11, 2024
Revised: November 6, 2024
Accepted: November 18, 2024
Published: January 13, 2025

https://doi.org/10.1021/acsnano.4c04795
ACS Nano 2025, 19, 3135–3146

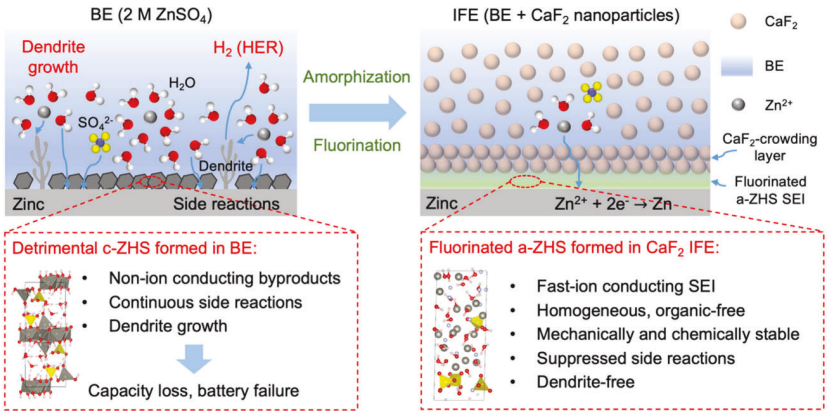

Figure 1. Schematic illustrations of the interphases formed on the zinc anode. Transformation of detrimental, non-ion conducting c-ZHS formed in the baseline electrolyte (BE) to fast-ion conducting, homogeneous, and stable fluorinated a-ZHS SEI formed in CaF_2 IFE (inorganically fluorinated electrolyte).

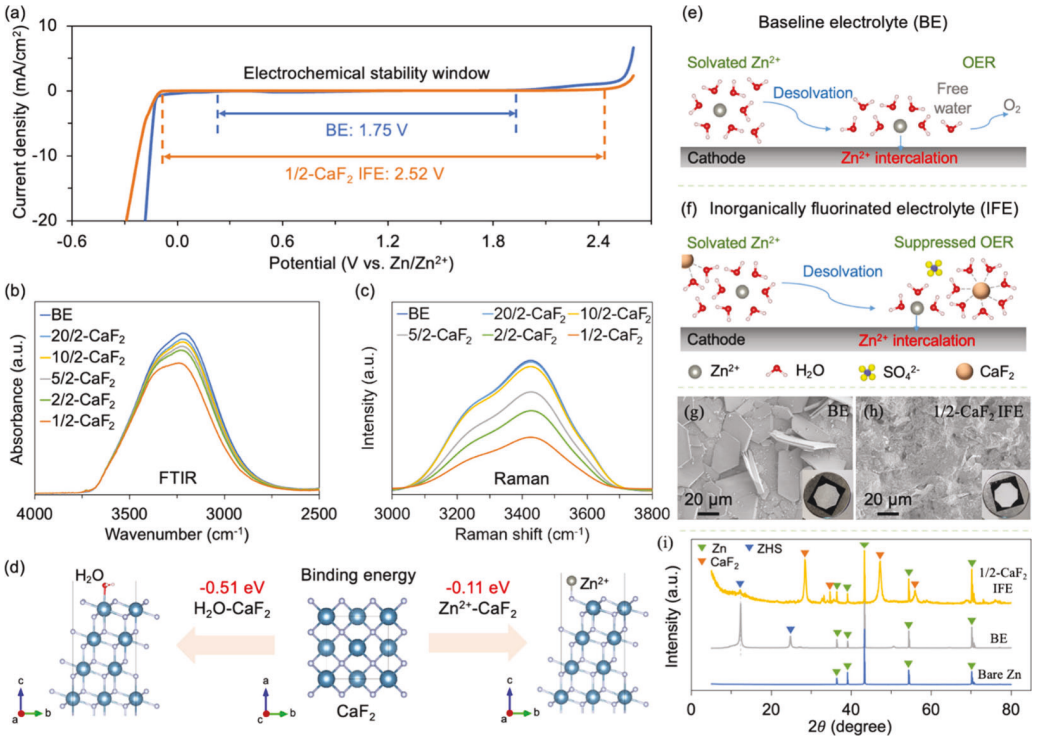

Figure 2. Electrolyte properties of IFEs. (a) ESW of BE and 1/2-CaF_2 of the IFE. (b) FTIR and (c) Raman spectra of BE and IFEs with different CaF_2 concentrations. (d) H_2O-CaF_2 and Zn^{2+}-CaF_2 binding energies. Schematics of the cathode/electrolyte interface in (e) BE and (f) 1/2-CaF_2 IFE. SEM and inserted optical images of zinc immersed in (g) BE and (h) 1/2-CaF_2 IFE for 15 days. (i) XRD patterns of bare zinc and aged zinc after the resting tests.

To prevent continuous HER and byproduct passivation, the rational design of a stable and Zn^{2+}-conductive solid-electrolyte interphase (SEI) on the zinc anode is essential. In prior work,[7−9] tremendous efforts have been dedicated to designing SEI based on the progressive decomposition of soluble organic species, similar to the evolution of SEIs in lithium batteries.[10] Although these in situ formed SEIs can kinetically increase the HER overpotential of water molecules and thus suppress byproduct formation, the progressive reduction of organic species on the anode surface inevitably leads to structural and compositional inhomogeneity and instability of the resulting organic-inorganic hybrid SEIs.[9] The heterogeneity of SEI can result in spatially nonuniform ion fluxes, inducing uneven metal plating/stripping and dendrite formation during cycling.[11,12] Moreover, the organic components in SEIs are insufficiently robust against the mechanical stresses induced by dendrites,[12] and their high solubility in the electrolytes can accelerate capacity losses due to SEI dissolution and regeneration.[13−15] Therefore, designing SEIs with homogeneous composition, stable structure, and excellent robustness is essential to the development of high-performance AZIBs.

Herein, contrary to the conventional belief that ZHS formation can only deteriorate the performance of AZIBs, we successfully transformed detrimental, non-ion conducting c-ZHS to fast-ion conducting fluorinated amorphous ZHS (a-ZHS) to in situ form a single-phase, stable SEI on zinc anode with enhanced electrochemical performance (Figure 1). The fluorinated a-ZHS was spontaneously formed on the zinc

https://doi.org/10.1021/acsnano.4c04795
ACS Nano 2025, 19, 3135−3146

anode in an inorganically fluorinated electrolyte (IFE) composed of a widely used sulfate baseline electrolyte (BE, 2 M $ZnSO_4$ in water unless specified) and CaF_2 nanoparticles. Its evolution follows the proposed mechanisms listed below:

$$2H_2O + 2e^- \rightarrow 2OH^- + H_2 \quad (3)$$

$$CaF_2 \rightleftarrows Ca^{2+} + 2F^- \quad (4)$$

$$4Zn^{2+} + xF^- + (6 - x)OH^- + SO_4^{2-} + yH_2O \rightarrow Zn_4(OH)_{6-x}F_xSO_4 \cdot yH_2O \text{ (amorphous)} \quad (5)$$

The key advantages of this amorphous SEI include: (1) fluorination and amorphization of ZHS substantially enhance its Zn^{2+} diffusion kinetics, making fluorinated a-ZHS highly Zn^{2+}-conductive; (2) fluorinated a-ZHS effectively prevents dendrite growth and side reactions between zinc and electrolytes after its formation; (3) fluorinated a-ZHS with homogeneous nanostructures and chemical compositions and high mechanical modulus minimizes the risks of SEI cracking and regeneration under stress; (4) fluorinated a-ZHS is organic-free and chemically stable, reducing capacity loss due to SEI dissolution and regeneration. The CaF_2 IFE also possesses an extended electrochemical stability window (ESW) of 2.52 V vs Zn/Zn^{2+}. Consequently, the stability of an AZIB full cell based on CaF_2 IFE is improved over 20,000 cycles at 3 A/g with a charging cutoff voltage of 2.2 V, substantially outperforming that (1,500 cycles) of the BE-based battery.

2. RESULTS AND DISCUSSION

2.1. Electrolyte Properties of the IFEs. To in situ construct the fluorinated a-ZHS SEI, the electrolytes were mixed with BE (e.g., 2 M $ZnSO_4$) and CaF_2 nanoparticles (Figure S1). The IFEs with liquid (BE)−solid (CaF_2) ratios of 20:2 and 1:2 were denoted as 20/2-CaF_2 and 1/2-CaF_2, respectively. As shown in Figure S2, among the CaF_2 IFEs, no liquid−solid phase separation was observed only in the gel-like 1/2-CaF_2 IFE after resting for 2 months under ambient conditions. When the solid content was further increased (e.g., 0.5/2-CaF_2 IFE), the resulting electrolyte displayed a dry and powdery texture, posing challenges for ion diffusions and cell assembling. Figures S3 and S4 show the viscosities and salt concentrations of the CaF_2 IFEs, respectively. Compared to BE, the 1/2-CaF_2 IFE exhibited a relatively high viscosity of 4.0 Pa·s and a lower $ZnSO_4$ concentration of 1.2 M at a high solid content of 38.6 vol % or 60.4 wt %. Nevertheless, as shown in Figure S5, the 1/2-CaF_2 IFE retained an ionic conductivity of 16.0 mS/cm, surpassing that (~8 mS/cm) of the water-in-salt electrolyte based on 21 m LiTFSI,[16] where m denotes mol/kg.

Other metal fluoride nanoparticles (e.g., LiF, ZnF_2, MgF_2; Figure S1) were added into BE for comparison with CaF_2 IFEs. Among these metal fluorides, concentrated CaF_2 nanoparticles exhibited the optimal effect in extending the electrochemical stability window of the IFEs as well as low cost and high abundance as shown in Figures S6 and S7. For instance, the 1/2-CaF_2 IFE exhibited an ESW of 2.52 V vs Zn/Zn^{2+} (Figure 2a), comparable to previously reported highly concentrated water-in-salt electrolytes, such as 21 m LiTFSI-1 m $Zn(OTf)_2$ (2.6 V vs Zn/Zn^{2+}) and 15 m KAc-10 m $Zn(Ac)_2$ (2.5 V vs Zn/Zn^{2+}).[17,18] In comparison, both LiF and ZnF_2 IFEs exhibited high OER activity above 1.90 V vs Zn/Zn^{2+} (Figure S7), implying fast OER-induced electrolyte depletion under high voltages. While the MgF_2 IFE exhibited higher HER and OER activities compared to the 1/2-CaF_2 IFE. In addition, the pH values of 1/2-CaF_2 and BE electrolytes were measured to be 3.51 and 4.2, respectively, indicating mild acidic conditions for both electrolytes. These results suggested that 1/2-CaF_2 IFE with suppressed water reactivity could be an ideal electrolyte for AZIBs. Moreover, the IFE exhibits superior cost advantages considering that natural CaF_2 (>97%) is available for approximately 0.4 USD/kg.[19]

Figure 2b shows the FTIR spectra of the CaF_2 IFEs. The intensity of the O−H stretching peak decreased with increasing CaF_2 concentrations, implying weakened H-bonding among water molecules and reduced water reactivity toward interfacial side reactions.[20] In comparison to other metal fluorides (Figure S8), CaF_2 nanoparticles demonstrated superior effectiveness in weakening H-bonding networks. The Raman spectra of the CaF_2 IFEs shown in Figure 2c further confirmed that water molecules were stabilized by CaF_2 nanoparticles, in good agreement with the phenomena observed in the FTIR spectra. Figure S9 displays the deconvolution of the O−H vibration peak of water molecules[20] to weak hydrogen bonds (H-bond) near 3,600 cm^{-1}, medium H-bond near 3,450 cm^{-1}, and strong H-bond near 3,250 cm^{-1}. The area ratios of the three deconvolution peaks remained relatively stable in the LiF, MgF_2, and CaF_2 IFEs. However, the area ratio of strong H-bond peak increased from 27.2% in BE to 50.2% in ZnF_2 IFE, correlating well with their pronounced OER activities (Figure S7).

Density functional theory (DFT) calculations were conducted to elucidate the influence of CaF_2 nanoparticles on water molecules in CaF_2 IFEs. As depicted in Figure 2d and Figure S10, the site near positively charged Ca atoms on CaF_2 (111) surface exhibited the most favorable water adsorption with a binding energy of −0.51 eV due to strong Coulombic attractions between positively charged Ca (CaF_2) and negatively charged O (H_2O). Therefore, reactive water molecules could be strongly absorbed and confined by CaF_2 nanoparticles through surface adsorption in the CaF_2 IFEs, leading to weakened H-bonding networks and thus reduced water reactivity.[21,22] For instance, as depicted in Figure S11, the free energy of hydrogen adsorption (a descriptor for HER[23]) significantly increased from 0.23 eV on Zn (101) surface to 1.32 eV on CaF_2 (111) surface. This suggested that the HER could be greatly suppressed on the CaF_2 surface, agreeing well with the higher HER overpotentials in CaF_2 IFEs. Meanwhile, the negatively charged F atoms on the CaF_2 surface contributed to stable Zn^{2+} adsorption with a binding energy of −0.11 eV, which could potentially alter the solvation structures and diffusion pathways of Zn^{2+} near the surface of CaF_2 nanoparticles. As illustrated in Figures 2e−f, the strong CaF_2−H_2O attractions also contributed to significantly suppressed the OER at the cathode/electrolyte interface, leading to extended cathodic limits of the CaF_2 IFEs. In addition, the highest occupied molecular orbital (HOMO) levels of $[Zn\cdot(H_2O)_6]^{2+}$ and $[Ca\cdot(H_2O)_6]^{2+}$ were calculated to examine the effect of CaF_2 on the solvation of Zn^{2+} (Figure S12 in Supporting Information). Figure S12 shows that $[Zn\cdot(H_2O)_6]^{2+}$ has a lower HOMO level compared to $[Ca\cdot(H_2O)_6]^{2+}$. It means that the solvation of Zn^{2+} would be relatively more preferred and stable than the solvation of Ca^{2+}, indicating that the effect of CaF_2 on the solvation of Zn would be negligible.

https://doi.org/10.1021/acsnano.4c04795
ACS Nano 2025, 19, 3135−3146

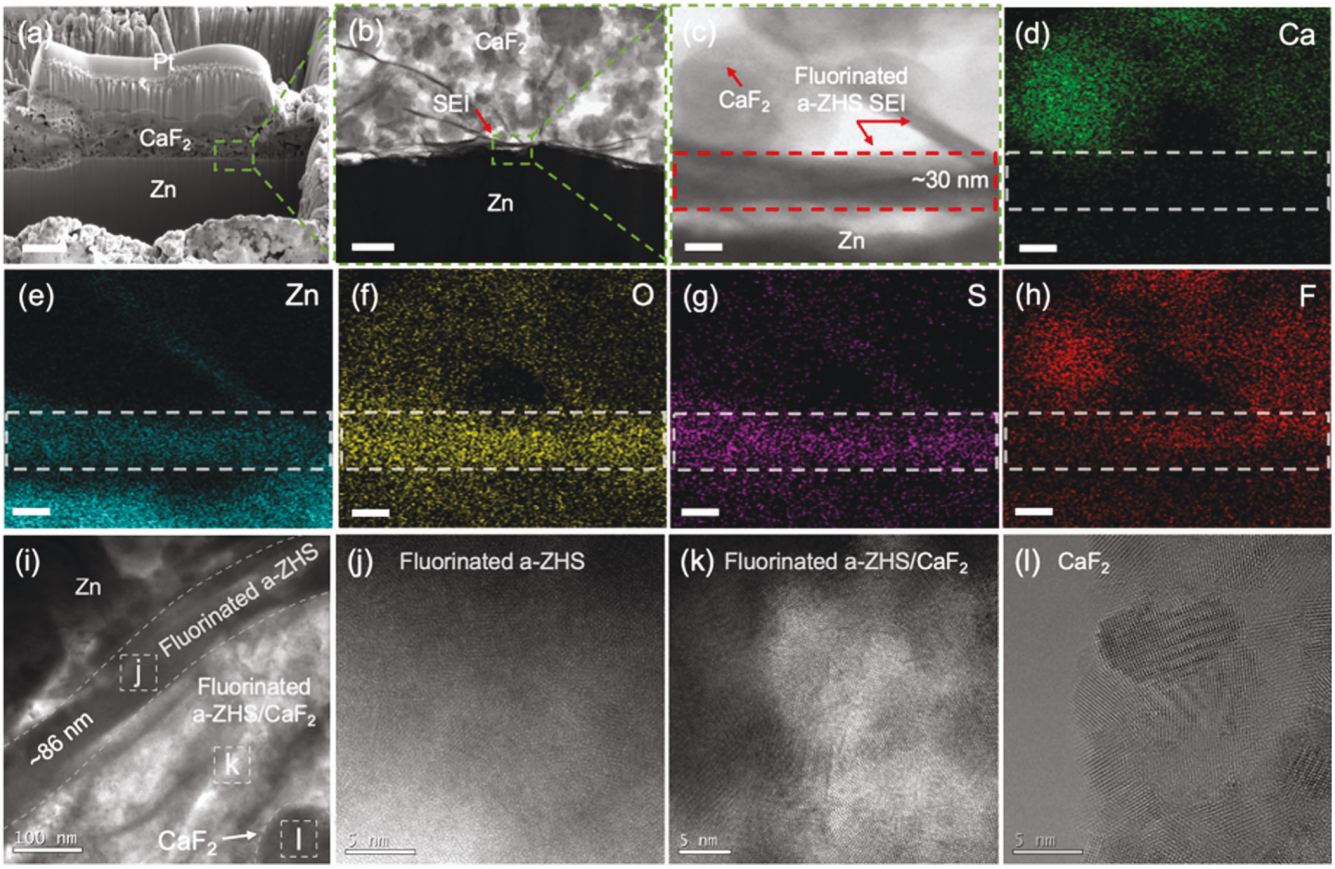

Figure 3. Nanostructures and chemical compositions of the fluorinated a-ZHS SEI. (a) Cross-sectional SEM image and (b)−(c) cross-sectional STEM image of zinc anode in a Zn||Zn symmetric cell with 1/2-CaF_2 IFE after the initial plating/stripping cycle. (d)−(h) Elemental mappings of fluorinated a-ZHS SEI on cycled zinc anode showing the distribution of Ca, Zn, O, S, and F. (i) TEM image of zinc anode in a Zn||Zn symmetric cell with 1/2-CaF_2 IFE after 10 plating/stripping cycles and (j)−(l) high-resolution TEM images of different regions. Scale bar: (a) 2 μm, (b) 300 nm, (c)−(h) 20 nm.

Figure S13 displays the Tafel curves of the zinc electrode tested in different electrolytes. The corrosion potential of the zinc electrode shifted from −9.7 mV in BE to −29.5 mV in 1/2-CaF_2 IFE, and the corrosion current density decreased from 12.6 to 3.1 mA/cm^2 (Figure S13a). These results indicated the significantly improved corrosion resistance of zinc due to low water contents and reduced water reactivity in 1/2-CaF_2 IFE. In other IFEs based on LiF, ZnF_2, and MgF_2, zinc corrosion was also effectively suppressed but more severe than that in the 1/2-CaF_2 IFE (Figure S13b). Furthermore, zinc foils were immersed in different electrolytes, including BE, CaF_2, LiF, ZnF_2, and MgF_2 IFEs for 15 days under ambient conditions. In comparison to bare zinc, the zinc immersed in BE was heavily passivated by large c-ZHS flakes (Figure 2g and Figures S14a−d) due to zinc corrosion, HER, and byproduct formation. As shown in Figure 2i, these c-ZHS byproducts displayed strong diffraction peaks located at 12.3°, 24.8°, and 50.8°. In sharp contrast, suspended CaF_2 nanoparticles in the IFE spontaneously formed a densely compacted layer on the zinc surface (Figure 2h and Figures S14e−f) after resting, and the characteristic diffraction peaks (Figure 2i) corresponding to CaF_2 at 28.4°, 47.2°, and 56.0° could be clearly identified.[24] Meanwhile, only a negligible c-ZHS peak existed at 12.3°, indicating that the spontaneously formed CaF_2 layer could effectively protect zinc from continuous corrosion and c-ZHS passivation in the sulfate electrolyte. Figures S14g−l and S15 provide SEM images and XRD patterns of the zinc foils immersed in other IFEs, respectively. These zinc foils suffered from pitting corrosion or c-ZHS passivation, suggesting that LiF, ZnF_2, and MgF_2 IFEs were less efficient in protecting zinc anodes since they failed to establish an effective SEI.

2.2. In Situ, Spontaneous Generation of the Fluorinated a-ZHS SEI. To investigate the nanostructures and chemical compositions of the SEI, cycled zinc anodes in Zn||Zn symmetric cells were characterized. As shown in Figure S16, an interphase layer with a morphology distinct from those of zinc and CaF_2 nanoparticles was spontaneously formed on the zinc anode after resting for 2 h in 1/2-CaF_2 IFE. Figure 3a shows the cross-sectional scanning electron microscopy (SEM) image of the zinc anode after the first plating/stripping cycle in the 1/2-CaF_2 IFE. A flat interface was observed between the zinc anode and the nanoporous CaF_2-crowding layer, indicating uniform zinc plating/stripping during cycling. Figure 3b−c presents the cross-sectional scanning transmission electron microscopy (STEM) images of the interface. The results clearly revealed the presence of a dense, flat SEI layer and a nanoporous CaF_2-crowding layer on the zinc anode. This in situ formed SEI layer was nearly free of Ca and mainly composed of Zn, O, and S (Figures 3d−g), agreeing well with the chemical composition of ZHS: $Zn_4(OH)_6SO_4{\cdot}xH_2O$. As shown in Figure 3h and Figure S18, the F element also existed in the SEI layer, indicating the fluorination of the in situ formed interphase. For the zinc anode after resting for 2 h (Figure S18) and 10 plating/stripping cycles (Figure S19), a

https://doi.org/10.1021/acsnano.4c04795
ACS Nano 2025, 19, 3135−3146

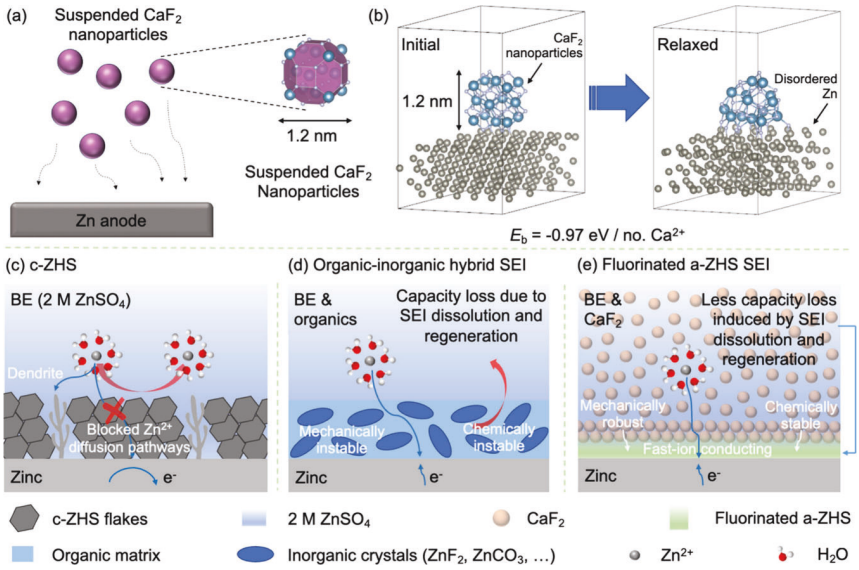

Figure 4. Analysis of c-ZHS, organic−inorganic hybrid SEI and fluorinated a-ZHS SEI. (a) Suspended CaF_2 nanoparticles near the zinc metal and (b) their atomic-scale configurations before and after relaxation. Schematic illustrations of (c) c-ZHS byproducts with sluggish Zn^{2+} diffusion kinetics formed in conventional sulfate electrolyte (i.e., 2 M $ZnSO_4$), (d) organic−inorganic hybrid SEIs with mechanical and chemical instability widely reported in prior work, and (e) mechanically robust, chemically stable, and organic-free fluorinated a-ZHS SEI formed in 1/2-CaF_2 IFE via the amorphization and fluorination of ZHS.

similar fluorinated SEI layer was observed, confirming the spontaneous formation of a fluorinated SEI on zinc anode when paired with 1/2-CaF_2 IFE.

As further revealed by the transmission electron microscopy (TEM) image shown in Figure 3i, three layers with distinct nanostructures were identified as Zn, ZHS, and CaF_2 nanoparticles and are separated by dashed lines. Note that the homogeneous and densely fluorinated ZHS region exhibited typical amorphous characteristics (Figure 3j). In the nanoporous CaF_2-crowding layer, both fluorinated a-ZHS and CaF_2 were observed, and the CaF_2 nanoparticles were well-connected in the presence of fluorinated a-ZHS (Figures 3k−l). This nanoporous CaF_2-crowding layer could serve as an additional, lean-liquid barrier to prevent side reactions between zinc and electrolytes when the fluorinated a-ZHS SEI undergoes potential damage during long-term cycling. Meanwhile, the abundant solid−liquid interfaces within this layer could ensure fast Zn^{2+} transport and uniform distribution of Zn^{2+} flux during charge/discharge.[25]

Figure S20 shows the surface morphology and elemental mappings of the zinc anode in a BE-based symmetric cell after 10 cycles. Numerous zinc dendrites with a representative height of approximately 45 μm were observed due to uneven zinc plating/stripping. Meanwhile, several c-ZHS byproduct flakes composed of Zn, O, and S elements were embedded in the porous zinc deposits, because of severe water-induced side reactions. In sharp contrast, a densely compacted layer of CaF_2 nanoparticles (Figure S21a) was in situ formed on the zinc anode cycled in 1/2-CaF_2 IFE. The thickness of this CaF_2-crowding layer reached approximately 20 μm after 10 cycles (Figure S21b), thinner than that (~35 μm) of precoated CaF_2 layer on zinc anode surface.[26] Figure S21 also indicates that 1/2-CaF_2 showed stable dendrite-free deposition of Zn covered by the CaF_2-crowding layer, while BE indicated very poor Zn plating accompanied by dendrites. It is inferred that dissolution of the cation−anion coordination reaction rarely occurs. The elemental mappings and X-ray photoelectron spectroscopy (XPS) shown in Figures S20c−d and Figure S22, respectively, confirmed that this nanoporous CaF_2-crowding layer predominately contains Ca and F.

Notably, CaF_2 nanoparticles play a key role in transforming c-ZHS in conventional sulfate electrolytes to fluorinated a-ZHS in the IFE. First, the fluorination of this SEI can be solely attributed to the slight dissolution of CaF_2 nanoparticles, which is completely different from those achieved via the decomposition of fluorine-containing organics or anions (e.g., BF_4^-, PF_6^-, $TFSI^-$, OTF^-) reported in prior work.[27,28] Furthermore, the binding energy between a suspended CaF_2 nanoparticle and zinc reached −0.97 eV/no. Ca^{2+} (Figures 4a−b). This introduced highly disordered zinc atoms on the anode surface, which could potentially serve as a template to facilitate the amorphization of ZHS. Importantly, the fluorinated a-ZHS SEI is in situ formed on the zinc anode in CaF_2 IFE due to the coordination between Zn^{2+} and anions (e.g., OH^-, F^-, and SO_4^{2-}). Therefore, the fluorinated a-ZHS SEI is self-healable during cycling, similar to the regeneration of SEIs widely observed in lithium batteries.[10] In comparison, a crystalline interface was observed between precoated CaF_2 and zinc with a smaller binding energy of −0.21 eV/no. Ca^{2+} (Figure S23). During cycling, precoated CaF_2 layers will lose their functionalities to protect zinc anode due to irreversible damages of the artificially introduced interface, leading to unsatisfactory battery performance.[26,29]

As schematically illustrated in Figures 4c−e, this fluorinated a-ZHS SEI is distinct from the interphases observed in conventional sulfate electrolytes and previously reported SEI-forming electrolytes.[8,27,28,30−34,57−59] In conventional sulfate electrolytes, spontaneously formed ZHS byproducts were highly crystallized and detrimental to battery performance. These non-ion conducting c-ZHS byproducts resulted in continuous anode passivation, electrolyte depletion, and dendrite growth between ZHS-covered surfaces. For other SEI-forming electrolytes,[8,27,28,30−34] the inorganic components in the resulting hybrid SEIs were also widely observed in a

https://doi.org/10.1021/acsnano.4c04795
ACS Nano 2025, 19, 3135−3146

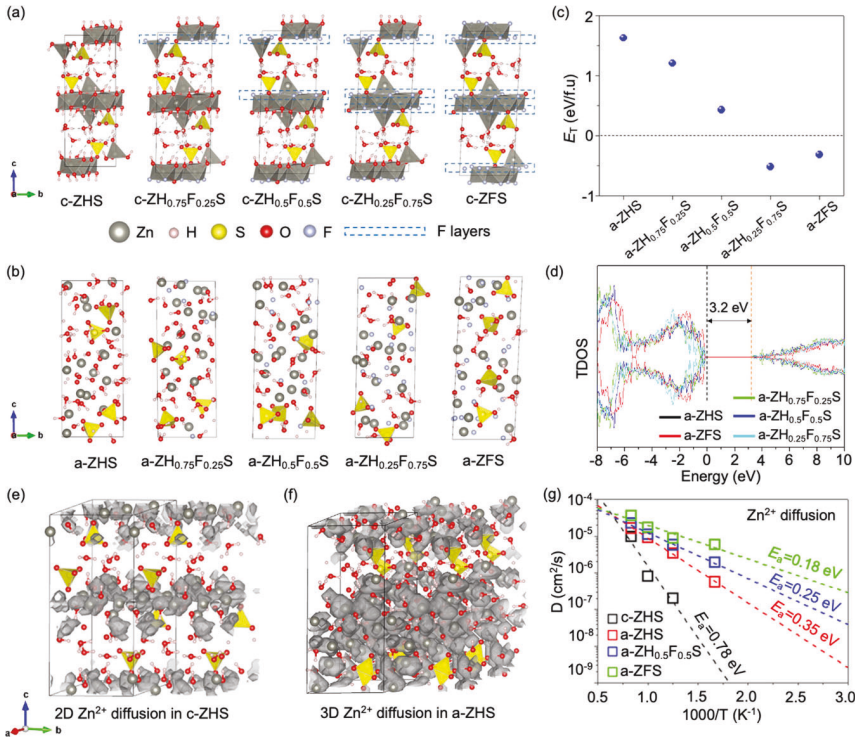

Figure 5. Fundamental physical properties of fluorinated a-ZHS. Atomic models of (a) c-$ZH_{1-x}F_xS$ and (b) a-$ZH_{1-x}F_xS$. (c) Crystalline-to-amorphous transition energy of a-$ZH_{1-x}F_xS$. (d) Total density of state (TDOS) of a-$ZH_{1-x}F_xS$. Trajectory of Zn^{2+} diffusion in (e) c-ZHS and (f) a-ZHS. (g) Activation energies of Zn^{2+} diffusion in c-ZHS, a-ZHS, a-$ZH_{0.5}F_{0.5}S$, and a-ZFS.

crystalline state although these crystalline inorganic materials are intrinsically nonconductive to ions (e.g., ZnF_2 with an ionic conductivity of 10^{-4} mS/cm[35]). Meanwhile, the organic components in these hybrid SEIs were poor in mechanical and chemical stability due to their low strength and high solubility.[12,15] In contrast, our current fluorinated a-ZHS SEI is highly amorphous and completely free of organic components. As summarized in Supplementary Table 1, ZHS exhibits a substantially lower solubility product of 10^{-57} in water[36] even compared with the inorganics (e.g., ZnF_2, ZnO, $ZnCO_3$) that have been widely observed in organic−inorganic hybrid SEIs.[8,27,28,30−34] Moreover, this design of SEI proves that the formation and fluorination of SEI in aqueous electrolytes do not necessarily need to rely on the decomposition of organics or anions but can be achieved via a simple HER-trigged cation−anion coordination.

2.3. Fundamental Physical Properties of Fluorinated a-ZHS. Due to the homogeneous nature of this single-phase SEI, density functional theory (DFT) calculations were conducted to systematically investigate the fundamental physical properties of fluorinated a-ZHS. A series of ZHS products with different degrees of F-substitution to the hydroxide (denoted as $ZH_{1-x}F_xS$, $0 \le x \le 1$) were considered. Figure 5a−b shows the atomic models of c-$ZH_{1-x}F_xS$ and a-$ZH_{1-x}F_xS$, respectively. As shown in Figure 5c, the crystalline-to-amorphous transition energies (E_T) of these $ZH_{1-x}F_xS$ products decreased with an increasing degree of F-substitution, suggesting the fluorine ions in the electrolytes could facilitate the amorphization of ZHS. Meanwhile, these a-$ZH_{1-x}F_xS$ products exhibited a similar band gap of 3.2 eV (Figure 5d), implying their electron-insulating properties since DFT calculations generally underestimate band gaps.[37]

Ab initio molecular dynamics (AIMD) simulations were performed to determine the activation energies (E_a) of Zn^{2+} diffusion in c-ZHS and a-$ZH_{1-x}F_xS$. Figure S24 shows the mean square displacement (MSD) of Zn^{2+} in c-ZHS and a-ZHS. The Zn^{2+} diffusion in c-ZHS mainly occurred within its in-plane and the cross-plane Zn^{2+} migration was highly prohibited, exhibiting a typical two-dimensional (2D) diffusion mode (Figure 5e). In contrast, the MSDs of Zn^{2+} along the in-plane and cross-plane directions of a-ZHS were comparable and were significantly higher than those observed in c-ZHS, indicating significantly enhanced Zn^{2+} diffusion. More importantly, as shown in Figure 5f, a-ZHS possessed three-dimensional (3D) Zn^{2+} diffusion pathways, which could be highly advantageous to facilitate fast ion transport across the SEI layer.

Figure 5g displays the activation energies of Zn^{2+} diffusion in c-ZHS and a-$ZH_{1-x}F_xS$. The c-ZHS possessed a high E_a of 0.78 eV. In comparison, the E_a in a-ZHS decreased to 0.35 eV and reached 0.18 eV when the a-ZHS was fully fluorinated (denoted as a-ZFS). Note that the E_a of a-ZHS is comparable to those of fast-ion conducting oxide solid electrolytes.[38] a-ZFS also exhibits an E_a similar to sulfide solid electrolytes, which are generally considered superionic conductors.[39] These results suggest that c-ZHS exhibits highly sluggish 2D Zn^{2+} transport kinetics, while a-ZHS is a 3D fast ion conductor to Zn^{2+}. Moreover, fluorination is highly beneficial to further enhancing Zn^{2+} diffusion in the amorphous SEI layer. Therefore, non-ion conducting c-ZHS blocks Zn^{2+} transport and prevents the ZHS-covered zinc surface from plating/stripping, leading to capacity loss and battery failure. In contrast, fast-ion conducting fluorinated a-ZHS could serve as a homogeneous and stable SEI layer to suppress dendrite growth and prevent

https://doi.org/10.1021/acsnano.4c04795
ACS Nano 2025, 19, 3135−3146

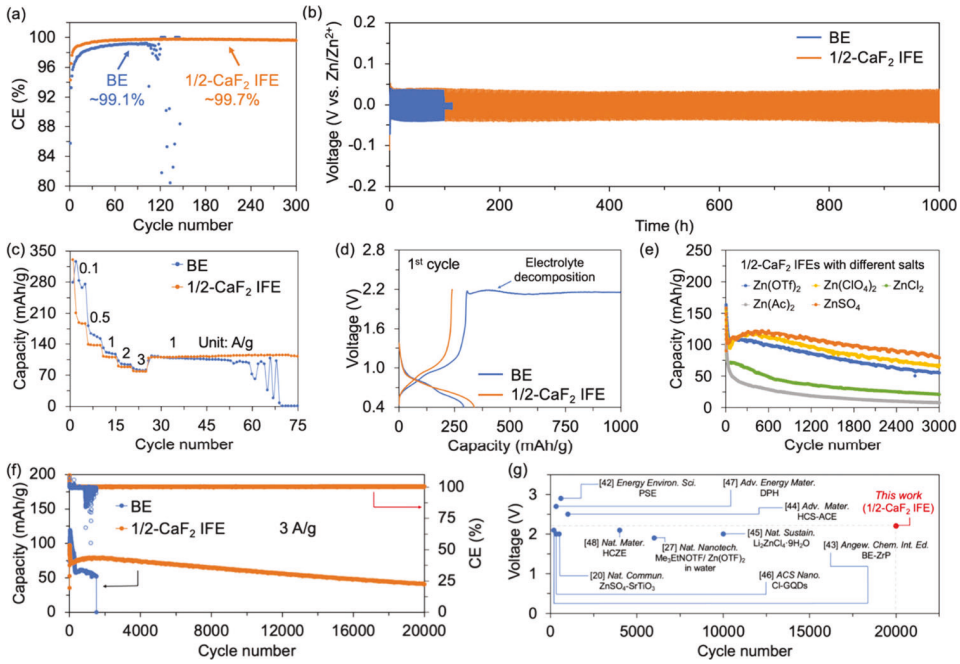

Figure 6. Electrochemical performance of 1/2-CaF_2 IFE in cells. (a) CEs of Cu||Zn asymmetric cells. (b) Cyclic stability of Zn||Zn symmetric cells. (c) Rate capability of Zn||NVO full cells at 1 A/g. (d) Voltage profiles of the 1st charge/discharge cycle of Zn||NVO full cells at 0.1 A/g. (e) Cyclic stability of Zn||NVO full cells with 1/2-CaF_2 IFE based on different zinc salts at 1 A/g. (f) Cyclic stability of Zn||NVO full cells at 3 A/g. (g) Comparisons of electrochemical performance of previously reported AZIBs based on different electrolytes.

continuous side reactions between zinc and aqueous electrolytes.

To understand the enhanced Zn^{2+} diffusion in a-ZHS, phonon dynamics of c-ZHS and a-ZHS were investigated via density functional perturbation theory (DFPT) calculations. Figure S25a exhibits the phonon density of states of c-ZHS and a-ZHS. The average phonon frequency (ω_{av}) decreased from 16.4 THz in c-ZHS to 14.0 THz in a-ZHS. Such decrease in ω_{av} of a-ZHS was mainly contributed by optical phonons ranging from 13 to 40 THz. This resulted in higher out-of-plane vibration amplitudes of the a-ZHS lattice, leading to a lower Zn^{2+} activation energy and higher Zn^{2+} mobility in a-ZHS given that atom migration is highly related to optical phonons.[40,41] Meanwhile, the spectra of acoustic phonons below ~13 THz were similar in c-ZHS and a-ZHS, agreeing well with their similar bulk modulus (c-ZHS: 19.1 GPa, a-ZHS: 17.2 GPa, Supplementary Figures 25b−c) as material rigidity mainly originates from the behavior of acoustic phonons.

2.4. Enhanced Electrochemical Performance of the CaF_2 IFE. To reveal the superior electrochemical performance of 1/2-CaF_2 IFE, Cu||Zn asymmetric cells and Zn||Zn symmetric cells were tested. As shown in Figure 6a, the CaF_2 IFE-based Cu||Zn asymmetric cell exhibited an initial Coulombic efficiency (CE) of 94.3%, significantly higher than that (85.8%) of the BE-based Cu||Zn cell. It is inferred that polarization is more related to the byproduct formation in BE than increase in viscosity induced by the incorporation of 1/2-CaF_2.[60] The CE of the CaF_2 IFE-based Cu||Zn asymmetric cell quickly reached above 99.7% with stable voltage profiles over 600 h (Figure S26), indicating high zinc plating/stripping reversibility in 1/2-CaF_2 IFE. In comparison, the CE of the BE-based Cu||Zn asymmetric cell stabilized around 99.1%, leading to its fast failure after approximately 100 cycles. Similarly, the cycle life of Zn||Zn symmetric cells was prolonged from 100 h with the BE to over 1,000 h with the 1/2-CaF_2 IFE (Figure 6b). Figure S27 shows the cyclic stability of Zn||Zn symmetric cells at 5 mAh/cm^2, indicating that the cycle life of 1/2-CaF_2 IFE-based cells was also enhanced at high depth of discharge compared to BE-based cells. In addition, Figure S28 shows typical crescent curves for BE and 1/2-CaF_2 IFE, indicating that no soft short occurred during Zn plating/stripping.[61] These results suggested that zinc anodes were highly stabilized in 1/2-CaF_2 IFE due to the formation of fluorinated a-ZHS SEI.

To further demonstrate the effectiveness of 1/2-CaF_2 IFE, widely reported sodium-doped vanadium oxide (NVO) and manganese dioxide/molybdenum oxide (MnO_2/MoO_3) were used as cathode materials to assemble full cells. All of the cells with an electrolyte volume of 80 μL were charged to 2.2 V to observe battery failure induced by dendrite growth and electrolyte depletion. As shown in Figure 6c, the CaF_2 IFE-based Zn||NVO full cell exhibited stable capacities of 186, 137, 110, 87, 77 mAh/g at current densities of 0.1, 0.5, 1, 2, 3 A/g, respectively. When the current density was recovered to 1 A/g, the capacity of the CaF_2 IFE-based full cell remained stable at approximately 110 mAh/g, indicating its superior rate capability and stability compared to those of the BE-based battery. In addition, the Zn||NVO full cell based on CaF_2 IFE exhibited capacities comparable to those based on BE even at a high current density of 3 A/g. It is inferred that Zn^{2+} diffuses fast through the fluorinated a-ZHS as calculated in Figure 5g. Electrochemical performance of Zn||NVO full cells was also evaluated at 0.5 A/g to validate the stability of cells based on 1/2-CaF_2 at small current densities. Figure S29 shows that the 1/2-CaF_2-based full cell maintains the capacity (approximately 150 mAh/g) quite well over 600 cycles, while the BE-based cell fails at around the 350th cycle. The cycling performance trend of Zn||NVO full cells tested at 0.5 A/g agrees well with that at 3 A/g, corroborating that 1/2-CaF_2 IFE is effective at

https://doi.org/10.1021/acsnano.4c04795
ACS Nano 2025, 19, 3135−3146

improving the cyclic stability of AZIBs at both small and high current densities. Figure 6d displays the first-cycle voltage profiles of these full cells at a current density of 0.1 A/g. Notably, the voltage of the BE-based full cell could only be charged to approximately 2.15 V due to severe electrolyte decomposition, in sharp contrast to the stable voltage profiles of the CaF_2 IFE-based battery. This confirmed that the electrolyte depletion induced by the oxygen evolution reaction at the cathode/electrolyte interface under increased voltages was also significantly suppressed by CaF_2 nanoparticles in the IFE.

Figure 6e shows the cyclic stability of the Zn||NVO full cells with the 1/2-CaF_2 IFEs based on different zinc salts, including $ZnSO_4$, $Zn(ClO_4)_2$, $ZnCl_2$, $Zn(Ac)_2$, and $Zn(OTf)_2$. Notably, in the presence of highly concentrated CaF_2 nanoparticles, the full cells with different zinc salts exhibited greatly enhanced stability (Figure S30). Among them, the 1/2-CaF_2 IFE based on 2 M $ZnSO_4$ exhibited optimal long-term stability over 3,000 cycles in full cells. The CaF_2 IFEs based on 2 M $Zn(ClO_4)_2$ and 2 M $Zn(OTf)_2$ electrolytes also demonstrated superior enhancement effects. These results provide strong evidence that the CaF_2 nanoparticles can be paired with different liquid electrolytes and zinc salts to further enhance the electrochemical performance of the AZIBs. At a higher current density of 3 A/g, the BE-based full cell underwent substantial capacity degradation and failed after approximately 1,500 cycles (Figure 6f). In contrast, the CaF_2 IFE-based battery exhibited excellent long-term stability and retained a capacity of 40.7 mAh/g after 20,000 cycles, substantially outperforming previously reported AZIBs,[20,27,42−48] as summarized in Figure 6g and Supplementary Table 2.

To validate the stability of 1/2-CaF_2 IFE, cycling tests of AZIB cells with high mass loading of NVO (>5 mg/cm^2) and high Zn utilization of thin Zn film (0.025 mm) were also examined (Figure S31). The CaF_2 IFE-based full cell with a high mass loading of NVO exhibits improved stability over 2,500 cycles, while the BE-based full cell with high mass loading of NVO shows short circuit at approximately the 1,200th cycle (Figure S31a). Figure S31b indicates that 1/2-CaF_2 IFE noticeably enhances the stability of AZIB cells with a thin Zn film, exhibiting much longer cycle life (>4,000 cycles) compared to that of BE-based AZIBs showing sudden failure at approximately the 2,300th cycle. It signifies that 1/2-CaF_2 IFE would improve the stability of the AIZBs regardless of the mass loading of NVO cathode materials. In particular, 1/2-CaF_2 IFE suppressed severe side reactions such as Zn dendrite effectively. Moreover, electrochemical tests show that the stability of 1/2-CaF_2 IFE was enhanced despite a relatively low pH compared to that of BE. It is inferred that the subtle difference in pH between 1/2-CaF_2 and BE would not affect cell performance. In addition, pouch cells were prepared and electrochemically characterized to validate the availability of 1/2-CaF_2 IFE to wide applications as shown in Figure S32. The cycling test shows a capacity retention of 80% over 100 cycles compared to the initial capacity, comparable to the performance of state-of-the-art pouch-cell AZIBs.[62−64] It is inferred that 1/2-CaF_2 can be applied to the pouch cell, exhibiting the potential for the commercialization of 1/2-CaF_2 IFE. Additionally, Figure S33 shows that the CaF_2 IFE-based Zn||MnO_2/MoO_3 battery also exhibited superior stability over 3,000 cycles at 1 A/g without introducing other electrolyte additives (e.g., $MnSO_4$[49]) to exclude the byproduct formation from additives. Meanwhile, the capacity of the BE-based Zn||MnO_2/MoO_3 battery quickly decayed to nearly zero after 1,500 cycles due to electrolyte dry-out. These results suggest the excellent stability and compatibility of the CaF_2 IFE when paired with different cathode materials. Compared to contemporary electrolyte systems reported in literature (Figure S34), such as dilute mild acidic electrolytes, water-in-salt electrolytes, and hybrid electrolytes, the CaF_2 IFE exhibits superior overall electrochemical performance. Given these advantages, the demonstration of the CaF_2 IFE and associated fluorinated a-ZHS SEI provides opportunities to further promote the battery performance.

3. CONCLUSIONS

A cost-effective, inorganically fluorinated electrolyte is formulated based on conventional sulfate electrolytes and CaF_2 nanoparticles, which successfully transforms the notoriously detrimental c-ZHS to a homogeneous fluorinated a-ZHS SEI. The evolution of the current SEI is based on a simple, spontaneous cation−anion coordination instead of intricate decomposition of organic molecules or anions in the electrolytes. Moreover, this fast-ion conducting, homogeneous SEI is organic-free and exhibits superior structural and chemical stability. Due to the effective suppression of side reactions and dendrite growth, the in situ formed SEI improves the reversibility of Zn plating/stripping in dilute and acidic aqueous electrolytes. Meanwhile, the concentrated CaF_2 nanoparticles effectively stabilize water molecules against electrochemical oxidation. With the CaF_2 IFE, AZIB full cells exhibit substantially improved stability over 20,000 cycles with a charging cutoff voltage of 2.2 V. Importantly, our electrolyte design strategy is demonstrated to be effective in battery systems containing a wide range of zinc salts and cathodes. This work elucidates the fundamental role of inorganic nanoparticles in electrolytes, providing useful guidelines for the rational design of advanced electrolyte systems and associated SEIs for high-performance batteries.

METHODS

Preparation of Electrolytes. The IFEs were prepared by mixing different metal fluoride nanoparticles with BE (2 M $ZnSO_4$ in water unless specified) in different liquid volume to solid mass ratios. For instance, the 20/2-CaF_2 IFE and 1/2-CaF_2 IFE were composed of 20 mL of BE with 2 g of CaF_2 and 1 mL of BE with 2 g of CaF_2, respectively. CaF_2 was provided by Thermo Scientific (CAS 7789-75-5). Based on the density of CaF_2, its concentration in 1/2-CaF_2 IFE is estimated to be 38.6 vol % or 60.4 wt %. The 1/2-CaF_2 IFE was selected as the optimal electrolyte; and the LiF, ZnF_2, and MgF_2 IFEs with the same liquid volume to solid mass ratio of 1:2 were prepared for comparison. The liquid−solid mixtures were mechanically mixed to prepare the IFEs. The CaF_2 IFEs with other BEs based on different zinc salts including $Zn(ClO_4)_2$, $ZnCl_2$, $Zn(Ac)_2$, and $Zn(OTf)_2$ were prepared following the same procedure.

Material Characterization. The material structures were analyzed by X-ray diffraction (XRD, Rigaku Ultima IV diffractometer), XPS (Versa Probe II), Fourier transformation infrared spectroscopy (FTIR, Agilent 660), and Raman spectroscopy (NRS-5100, Jasco). The rheological properties of the BE and IFEs were measured by a rotational rheometer (Discovery HR-2, TA Instruments) using a stainless-steel Peltier plate (8 mm). The ionic conductivity of the IFEs and pH were measured by a conductivity meter (EC600, EXTECH). Scanning electron microscopy (Sigma 500 VP, Zeiss) with an energy-dispersive X-ray spectroscopy (EDAX) probe was utilized to characterize the surface morphologies and elemental distributions of the zinc anode. Focused ion beam (FIB)/

https://doi.org/10.1021/acsnano.4c04795
ACS Nano 2025, 19, 3135−3146

SEM (FEI, Nova 200) with a nanomanipulator was employed to prepare the sample for TEM/STEM, JEM-ARM200F.

Cell Assembling. Standard CR2032 coin cell was used for assembling cells. Zinc discs with a thickness of 0.08 mm and a diameter of 14 mm were used as the anode. Glass fiber membrane with a thickness of 250 μm (GF/A, Whatman) and a diameter of 16 mm was used as the separator. Pouch cells with a 5 cm × 6 cm size were prepared with electrodes (3.5 cm × 3.5 cm) and glass fiber membrane separator (4 cm × 4 cm). Aluminum and nickel taps were used for terminals for the positive and negative electrodes, respectively. The cathode material, NVO, and MnO_2/MoO_3 were prepared following the procedures described in prior work.[50,51] The active material, carbon black, and binder (PVDF) were mixed in a weight ratio of 7:2:1 and ground with NMP to form a slurry. Then, the slurry was uniformly coated on carbon paper and dried under a vacuum at 80 °C overnight. The mass loading was 2−3 mg/cm^2. Finally, cathode electrodes were obtained by punching the coated carbon paper into Φ14 mm discs and were used as the cathode for assembling full cells. 80 μL of the BE or IFEs was used in all the cells.

Electrochemical Measurements. All of the cells were rested for 2 h before electrochemical tests. The linear sweep voltammetry (LSV), chromatoamperometry (CA), and Tafel tests were conducted on an electrochemical workstation (Interface 1010E, Gamry). Among them, LSV (−0.5 to 2.6 V vs Zn/Zn^{2+}, 5 mV/s) and CA tests were performed using Zn||stainless steel (SS) asymmetric cells. LSV measurements were carried out at a sweep rate of 5 mV/s from −0.5 to 2.6 V to characterize hydrogen and oxygen evolution reactions. During the CA tests, a constant overpotential of −150 mV was applied to the Zn|SS asymmetric cells. Tafel tests were performed using Zn||Zn symmetric cells with a voltage window between −300 to 300 mV vs the open circuit potential at a scan rate of 1 mV/s. Galvanostatic charge/discharge tests were performed on a multichannel battery testing system (NEWARE).

DFT Calculations. The atomic and electronic structures were analyzed by using DFT calculations. All DFT calculations were conducted by using the Vienna Ab Initio Simulation Package (VASP) implementing the exchange-correlation functional of the spin-polarized generalized gradient approximation (GGA) parametrized by Perdew−Burke−Ernzerhof (PBE).[52] Structures of bulk ZHS, zinc metal, and CaF_2 nanoparticles were constructed based on Monkhorst−Pack grid of 4×4×1, 4×6×1 and Gamma-centered grid of 2×2×1, 1×1×1 k-point grids with a cutoff energy of 500 eV, respectively. Hubbard U value of 7.0 eV was adopted for the Zn in ZHS to introduce the strong d-electron band correlations.[53] All the structures were fully relaxed for thermodynamic stabilization, and van der Waals interaction was also introduced during calculations.

The binding energies (E_b) between CaF_2−H_2O and CaF_2−Zn^{2+} were calculated according to eq 6:

$$E_b = E_{total}(CaF_2{-}Zn^{2+}\text{ or }H_2O) + n_1E_{total}(H_2O) - E_{total}(CaF_2) - n_2E_{total}(Zn^{2+}) \quad (6)$$

where $E_{total}(CaF_2{-}Zn^{2+}\text{ or }H_2O)$ is the total energy of Zn^{2+} or H_2O adsorption onto CaF_2, $E_{total}(H_2O)$ is the energy of H_2O molecule, n_1 and n_2 are the numbers of H_2O molecule and Zn^{2+}, $E_{total}(CaF_2)$ is the energy for the surface of CaF_2 and $E_{total}(Zn^{2+}\text{ or }H_2O)$ is the energy of Zn^{2+} solvated by H_2O molecules. The binding energies between precoated CaF_2−Zn and suspended CaF_2−Zn systems were calculated according to eqs 7 and 8, respectively:

$$E_{b_{pre\text{-}coated}} = E_{total}(interface) - E_{total}(Zn(001)) - E_{total}(CaF_2(111)) \quad (7)$$

$$E_{b_{suspended}} = E_{total}(Zn(111) - CaF_2(NP)) - E_{total}(Zn(111)) - E_{total}(CaF_2(NP)) \quad (8)$$

where E_{total}(interface), E_{total}(Zn), $E_{total}(CaF_2)$, and $E_{total}(CaF_2(NP))$ are the total energy of the interface, Zn (001) surface, bulk CaF_2 (111) surface and CaF_2 nanoparticle (NP), respectively. A surface strain of ∼5% was introduced to construct a periodic interface. The crystalline-to-amorphous transition energies (E_T) of $ZH_{1-x}F_xS$ structures were calculated according to eq 9:

$$E_T = E_{total}(a\text{-}ZH_{1-x}F_xS) - E_{total}(c\text{-}ZH_{1-x}F_xS) \quad (9)$$

where E_T is the total energy of each structure.

Gibbs Free Energy of HER. The Volmer mechanism ($H^+ + e^- \rightarrow H^*$) was considered to describe the HER. The H* symbol is the adsorbed H on the surface model. The Gibbs free energy of H* adsorption (ΔG) was calculated according to eq 10:[23]

$$\Delta G = \Delta E + \Delta E_{ZPE} - T\Delta S \quad (10)$$

where ΔE, ΔE_{ZPE}, T, and ΔS are the adsorption energy of H atom, zero-point energy (ZPE), temperature, and entropy variation, respectively.

Phonon Dynamics. Phonon spectra were calculated by DFPT using VASP with a Gamma-centered k-point for c-ZHS and a-ZHS. The atomic structures were relaxed when all atomic forces were less than 10^{-7} eV/Å. The phonon density of states (PDOS) were examined by phonopy package with interatomic forces and atomic position obtained from DFPT.[54] The average phonon frequency (ω_{av}) was calculated according to eq 11:

$$\omega_{av} = \frac{\int \omega \mathrm{PDOS}(\omega)\mathrm{d}\omega}{\int \mathrm{PDOS}(\omega)\mathrm{d}\omega} \quad (11)$$

The bulk modulus of c-ZHS and a-ZHS were calculated via the Birch−Murnaghan equation of state (EOS) according to eq 12:[55]

$$E_{total}(V) = E_0 + \frac{9V_0B_0}{16}\left\{\left[\left(\frac{V}{V_0}\right)^{2/3} - 1\right]^3 B_0' + \left[\left(\frac{V}{V_0}\right)^{2/3} - 1\right]^2 \left[6 - 4\left(\frac{V}{V_0}\right)^{2/3}\right]\right\} \quad (12)$$

where $E_{total}(V)$ is the internal energy, E_0 is the equilibrium energy, V is the changed volume, V_0 is the equilibrium volume, B_0 is the bulk modulus and B_0' is the first derivative of the bulk modulus.

AIMD. The AIMD method was employed to construct a-ZHS by the melt-quenching (MQ) method. Canonical (NVT) ensemble with a Nose−Hoover thermostat and a Gamma-centered k-point was introduced for the AIMD simulation. The c-ZHS and fluorinated c-ZHS were first melted at 3,500 K for 5,000 timesteps (5 ps). Then, the melted structures were quenched to 100 K at a cooling rate of 200 K/ps. The quenched structures were equilibrated at 300 K for 5 ps before calculations.

The kinetics of Zn^{2+} diffusions in c-ZHS, a-ZHS and fluorinated a-ZHS were examined by AIMD simulations. The c-ZHS was examined at the desired temperatures ranging from 800 to 1,200 K for 10 ps. The a-ZHS and fluorinated a-ZHS were examined at the desired temperatures ranging from 600 to 1,200 K for 5 ps. A longer simulation time was needed to facilitate the thermal activation of c-ZHS due to its sluggish ion diffusions. The diffusion coefficient (D) was calculated based on the linear fit of the MSD over time according to eq 13:[56]

$$D = \frac{1}{2dt}\langle[\Delta r(t)]^2\rangle \quad (13)$$

where d is a dimensional factor and d equals 3 for 3D structures, t is the time duration for the simulation, and $[\Delta r(t)]^2$ is the MSD. Particularly, the MSD was calculated according to eq 14:

$$[\Delta r(t)]^2 = \frac{1}{N}\sum_i^N \langle[r_i(t + t_0)]^2 - [r_i(t_0)]^2\rangle \quad (14)$$

where $r_i(t)$ is the displacement of the i^{th} Zn-ion at time t and N is the total number of Zn^{2+}.

https://doi.org/10.1021/acsnano.4c04795
ACS Nano 2025, 19, 3135−3146

The activation energies (E_a) of Zn^{2+} diffusion in c-ZHS and a-$ZH_{1-x}F_xS$ were determined based on the diffusion coefficient (D) and the Arrhenius equation:

$$D = D_0 \exp\left(-\frac{E_a}{kT}\right) \quad (15)$$

where D_0 is the highest diffusivity at infinite temperature, k is the Boltzmann constant, and T is the temperature.

ASSOCIATED CONTENT

Supporting Information

The Supporting Information is available free of charge at https://pubs.acs.org/doi/10.1021/acsnano.4c04795.

Optical images of electrolytes; Viscosity, salt concentration, and ionic conductivity measurements; Materials characterization such as FTIR, Raman, XPS, SEM, STEM, XRD, and elemental mapping; Electrochemical characterizations including ESW tests of electrolytes and stability tests of symmetric cells, asymmetric cells, coin full cells and pouch full cells; Simulations of localization function (ELF), charge states, mean square displacement, phonon density of states, and bulk modulus (PDF)

AUTHOR INFORMATION

Corresponding Authors

Guoping Xiong − *Department of Mechanical Engineering, The University of Texas at Dallas, Richardson, Texas 75080, United States;* orcid.org/0000-0002-3216-0506; Email: guoping.xiong@utdallas.edu

Kyeongjae Cho − *Department of Material Science Engineering, The University of Texas at Dallas, Richardson, Texas 75080, United States;* orcid.org/0000-0003-2698-7774; Email: kjcho@utdallas.edu

Authors

Siyu Tian − *Department of Mechanical Engineering, The University of Texas at Dallas, Richardson, Texas 75080, United States;* orcid.org/0000-0001-6463-0691

Taesoon Hwang − *Department of Material Science Engineering, The University of Texas at Dallas, Richardson, Texas 75080, United States;* orcid.org/0000-0002-1264-1265

Zhuoxun Zhang − *Department of Mechanical Engineering, The University of Texas at Dallas, Richardson, Texas 75080, United States;* orcid.org/0009-0009-8666-7853

Shiwen Wu − *Department of Mechanical Engineering, The University of Texas at Dallas, Richardson, Texas 75080, United States*

Amirarsalan Mashhadian − *Department of Mechanical Engineering, The University of Texas at Dallas, Richardson, Texas 75080, United States*

Renzheng Zhang − *Aerospace and Mechanical Engineering, University of Notre Dame, Indiana 46556, United States*

Tye Milazzo − *Aerospace and Mechanical Engineering, University of Notre Dame, Indiana 46556, United States*

Tengfei Luo − *Aerospace and Mechanical Engineering, University of Notre Dame, Indiana 46556, United States;* orcid.org/0000-0003-3940-8786

Ruda Jian − *Department of Mechanical Engineering, The University of Texas at Dallas, Richardson, Texas 75080, United States*

Tianyi Li − *X-ray Science Division, Argonne National Laboratory, Lemont, Illinois 60439, United States;* orcid.org/0000-0002-6234-6096

Complete contact information is available at: https://pubs.acs.org/10.1021/acsnano.4c04795

Author Contributions

#Siyu Tian and Taesoon Hwang contributed equally.

Author Contributions

S.T., G.X., K.C., and T.H. conceived the idea. S.T. designed the experiments involved in the study including viscosity, Raman, FTIR, XRD, XPS, EDAX, SEM, FIB-SEM, TEM analyses, electrochemical measurements, and battery tests. T.H. contributed to simulations (DFT, AIMD, and DFPT) and experiments (material synthesis, SEM, pH, assembly and electrochemical tests of coin/pouch cells.). Z.Z. contributed characterization and stability analyses of coin/pouch cell. S.W. contributed to SEM analysis. A.M. contributed to XRD analysis. R.Z. and T.F.L. contributed to Raman tests. T.M. and T.F.L. contributed to viscosity measurements. R.J. contributed to optimizing cathode materials. T.Y.L. contributed to the battery design. All authors discussed and analyzed the data. S.T., G.X, K.C., and T.H. cowrote and revised the paper. G.X. and K.C. supervised the work.

Notes

The authors declare no competing financial interest.

ACKNOWLEDGMENTS

G.X. thanks the University of Texas at Dallas (UTD) startup fund, and G.X. and K.C. acknowledge the UTD internal battery funding and the support from the NSF (Grant No. 2324593). The authors acknowledge Dr. Josefina Arellano from the Department of Materials Science and Engineering for her assistance in FIB, STEM, and TEM characterization.

REFERENCES

(1) Fang, G.; Zhou, J.; Pan, A.; Liang, S. Recent advances in aqueous zinc-ion batteries. *ACS Energy Lett.* **2018**, *3*, 2480−2501.

(2) Chao, D.; Zhou, W.; Xie, F.; Ye, C.; Li, H.; Jaroniec, M.; Qiao, S.-Z. Roadmap for advanced aqueous batteries: From design of materials to applications. *Sci. Adv.* **2020**, *6*, No. eaba4098.

(3) Shin, J.; Lee, J.; Park, Y.; Choi, J. W. Aqueous zinc ion batteries: focus on zinc metal anodes. *Chem. Sci.* **2020**, *11*, 2028−2044.

(4) Yang, W.; Yang, Y.; Yang, H.; Zhou, H. Regulating water activity for rechargeable zinc-ion batteries: Progress and perspective. *ACS Energy Lett.* **2022**, *7*, 2515−2530.

(5) Lim, W.-G.; Li, X.; Reed, D. Understanding the role of zinc hydroxide sulfate and its analogues in mildly acidic aqueous zinc batteries: A review. *Small Methods* **2024**, *8*, No. 2300965.

(6) Wu, D.; et al. Simultaneous elucidation of solid and solution manganese environments via multiphase operando extended X-ray absorption fine structure spectroscopy in aqueous Zn/MnO_2 batteries. *J. Am. Chem. Soc.* **2022**, *144*, 23405−23420.

(7) Li, Y.; Yu, Z.; Huang, J.; Wang, Y.; Xia, Y. Constructing solid electrolyte interphase for aqueous zinc batteries. *Angew. Chem., Int. Ed.* **2023**, *62*, No. e202309957.

(8) Ma, L.; et al. Critical factors dictating reversibility of the zinc metal anode. *Energy Environ. Mater.* **2020**, *3*, 516−521.

(9) Sui, Y.; Ji, X. Electrolyte interphases in aqueous batteries. *Angew. Chem., Int. Ed.* **2024**, *63*, No. e202312585.

(10) Heiskanen, S. K.; Kim, J.; Lucht, B. L. Generation and evolution of the solid electrolyte interphase of lithium-ion batteries. *Joule* **2019**, *3*, 2322−2333.

(11) Lin, D.; Liu, Y.; Cui, Y. Reviving the lithium metal anode for high-energy batteries. *Nat. Nanotechnol.* **2017**, *12*, 194−206.
(12) Zhang, Q.-K.; et al. Homogeneous and mechanically stable solid−electrolyte interphase enabled by trioxane-modulated electrolytes for lithium metal batteries. *Nat. Energy* **2023**, *8*, 725−735.
(13) Mogensen, R.; Brandell, D.; Younesi, R. Solubility of the solid electrolyte interphase (SEI) in sodium ion batteries. *ACS Energy Lett.* **2016**, *1*, 1173−1178.
(14) Jin, Y.; et al. Low-solvation electrolytes for high-voltage sodium-ion batteries. *Nat. Energy* **2022**, *7*, 718−725.
(15) Sayavong, P.; et al. Dissolution of the solid electrolyte interphase and its effects on lithium metal anode cyclability. *J. Am. Chem. Soc.* **2023**, *145*, 12342−12350.
(16) Xiao, D.; Dou, Q.; Zhang, L.; Ma, Y.; Shi, S.; Lei, S.; Yu, H.; Yan, X. Optimization of organic/water hybrid electrolytes for high-rate carbon-based supercapacitor. *Adv. Funct. Mater.* **2019**, *29*, No. 1904136.
(17) Wan, F.; et al. Reversible oxygen redox chemistry in aqueous zinc-ion batteries. *Angew. Chem., Int. Ed.* **2019**, *58*, 7062−7067.
(18) Dong, D.; Wang, T.; Sun, Y.; Fan, J.; Lu, Y.-C. Hydrotropic solubilization of zinc acetates for sustainable aqueous battery electrolytes. *Nat. Sustain.* **2023**, *6*, 1474.
(19) Xiao, A. W.; Galatolo, G.; Pasta, M. The case for fluoride-ion batteries. *Joule* **2021**, *5*, 2823−2844.
(20) Deng, R.; He, Z.; Chu, F.; Lei, J.; Cheng, Y.; Zhou, Y.; Wu, F. An aqueous electrolyte densified by perovskite $SrTiO_3$ enabling high-voltage zinc-ion batteries. *Nat. Commun.* **2023**, *14*, 4981.
(21) Tian, S.; et al. Suppressing dendrite growth and side reactions via mechanically robust laponite-based electrolyte membranes for ultrastable aqueous zinc-ion batteries. *ACS Nano* **2023**, *17*, 14930−14942.
(22) Tian, S.; Hwang, T.; Malakpour Estalaki, S.; Tian, Y.; Zhou, L.; Milazzo, T.; Moon, S.; Wu, S.; Jian, R.; Balkus, K.; et al. A Low-Cost Quasi-Solid-State "Water-in-Swelling-Clay" Electrolyte Enabling Ultrastable Aqueous Zinc-Ion Batteries. *Adv. Energy Mater.* **2023**, *13*, No. 2300782.
(23) Nørskov, J. K.; et al. Trends in the exchange current for hydrogen evolution. *J. Electrochem. Soc.* **2005**, *152*, J23.
(24) Chingo Aimacaña, C. M.; et al. Bimodal ultrasound and X-ray bioimaging properties of particulate calcium fluoride biomaterial. *Molecules* **2021**, *26*, 5447.
(25) Wang, W.; Chen, S.; Liao, X.; Huang, R.; Wang, F.; Chen, J.; Wang, Y.; Wang, F.; Wang, H. Regulating interfacial reaction through electrolyte chemistry enables gradient interphase for low-temperature zinc metal batteries. *Nat. Commun.* **2023**, *14*, 5443.
(26) Li, Y.; et al. A stable fluoride-based interphase for a long cycle Zn metal anode in an aqueous zinc ion battery. *J. Mater. Chem. A* **2022**, *10*, 14399−14410.
(27) Cao, L.; et al. Fluorinated interphase enables reversible aqueous zinc battery chemistries. *Nat. Nanotechnol.* **2021**, *16*, 902−910.
(28) Meng, C.; et al. A eutectic electrolyte for an ultralong-lived $Zn//V_2O_5$ cell: an in situ generated gradient solid-electrolyte interphase. *Energy Environ. Sci.* **2023**, *16*, 3587−3599.
(29) Feng, Y.; Wang, Y.; Sun, L.; Zhang, K.; Liang, J.; Zhu, M.; Tie, Z.; Jin, Z. Fluorinated interface engineering toward controllable zinc deposition and rapid cation migration of aqueous Zn-ion batteries. *Small* **2023**, *19*, No. 2302650.
(30) Yang, J.; Zhang, Y.; Li, Z.; Xu, X.; Su, X.; Lai, J.; Liu, Y.; Ding, K.; Chen, L.; Cai, Y.-P.; et al. Three birds with one stone: tetramethylurea as electrolyte additive for highly reversible Zn-metal anode. *Adv. Funct. Mater.* **2022**, *32*, No. 2209642.
(31) Zhang, W.; He, G. Solid-electrolyte interphase chemistries towards high-performance aqueous zinc metal batteries. *Angew. Chem., Int. Ed.* **2023**, *62*, No. e202218466.
(32) Liang, G.; Tang, Z.; Han, B.; Zhu, J.; Chen, A.; Li, Q.; Chen, Z.; Huang, Z.; Li, X.; Yang, Q.; et al. Regulating inorganic and organic components to build amorphous-ZnF_x enriched solid-electrolyte interphase for highly reversible Zn metal chemistry. *Adv. Mater.* **2023**, *35*, No. 2210051.
(33) Wang, D.; Lv, D.; Peng, H.; Wang, C.; Liu, H.; Yang, J.; Qian, Y. Solvation modulation enhances anion-derived solid electrolyte interphase for deep cycling of aqueous zinc metal batteries. *Angew. Chem., Int. Ed.* **2023**, *62*, No. e202310290.
(34) Han, D.; et al. A non-flammable hydrous organic electrolyte for sustainable zinc batteries. *Nat. Sustain.* **2022**, *5*, 205−213.
(35) Han, J.; et al. A thin and uniform fluoride-based artificial interphase for the zinc metal anode enabling reversible Zn/MnO_2 batteries. *ACS Energy Lett.* **2021**, *6*, 3063−3071.
(36) Boshkov, N.; Petrov, K.; Vitkova, S.; Raichevsky, G. Galvanic alloys Zn-Mn-composition of the corrosion products and their protective ability in sulfate containing medium. *Surf. Coat. Technol.* **2005**, *194*, 276−282.
(37) Xiao, H.; Tahir-Kheli, J.; Goddard, W. A., III Accurate band gaps for semiconductors from density functional theory. *J. Phys. Chem. Lett.* **2011**, *2*, 212−217.
(38) Wang, Y.; et al. Design principles for solid-state lithium superionic conductors. *Nat. Mater.* **2015**, *14*, 1026−1031.
(39) Hwang, T.; Conlin, P.; Cho, M.; Cho, K. Electrochemical stability and Li ion diffusion kinetics of grain boundaries in $Li_{10}GeP_2S_{12}$ solid electrolyte. *J. Phys. Chem. C* **2023**, *127*, 7528−7535.
(40) Wakamura, K. Roles of phonon amplitude and low-energy optical phonons on superionic conduction. *Phys. Rev. B* **1997**, *56*, 11593.
(41) Muy, S.; Schlem, R.; Shao-Horn, Y.; Zeier, W. G. Phonon−ion interactions: Designing ion mobility based on lattice dynamics. *Adv. Energy Mater.* **2021**, *11*, No. 2002787.
(42) Chen, A.; et al. An immiscible phase-separation electrolyte and interface ion transfer electrochemistry enable zinc/lithium hybrid batteries with a 3.5 V-class operating voltage. *Energy Environ. Sci.* **2023**, *16*, 4054−4064.
(43) Peng, H.; Wang, C.; Wang, D.; Song, X.; Zhang, C.; Yang, J. Dynamic Zn/electrolyte interphase and enhanced cation transfer of sol electrolyte for all-climate aqueous zinc metal batteries. *Angew. Chem., Int. Ed.* **2023**, *62*, No. e202308068.
(44) Zhou, A.; Zhang, J.; Chen, M.; Yue, J.; Lv, T.; Liu, B.; Zhu, X.; Qin, K.; Feng, G.; Suo, L. An electric-field-reinforced hydrophobic cationic sieve lowers the concentration threshold of water-in-salt electrolytes. *Adv. Mater.* **2022**, *34*, No. 2207040.
(45) Yang, C.; et al. All-temperature zinc batteries with high-entropy aqueous electrolyte. *Nat. Sustain.* **2023**, *6*, 325−335.
(46) Wang, H.; et al. Bifunctional dynamic adaptive interphase reconfiguration for zinc deposition modulation and side reaction suppression in aqueous zinc ion batteries. *ACS Nano* **2023**, *17*, 11946−11956.
(47) Qin, T.; Li, K.; Liu, Y.; Xu, Z.; Gao, C. Low-concentration hydrogel polyelectrolyte with in situ formed interphases enables 2.7 V aqueous pouch cell. *Adv. Energy Mater.* **2023**, *13*, No. 2300733.
(48) Wang, F.; et al. Highly reversible zinc metal anode for aqueous batteries. *Nat. Mater.* **2018**, *17*, 543−549.
(49) Wu, B.; Zhang, G.; Yan, M.; Xiong, T.; He, P.; He, L.; Xu, X.; Mai, L. Graphene scroll-coated α-MnO_2 nanowires as high-performance cathode materials for aqueous Zn-ion battery. *Small* **2018**, *14*, No. 1703850.
(50) Zhou, J.; Zhang, L.; Peng, M.; Zhou, X.; Cao, Y.; Liu, J.; Shen, X.; Yan, C.; Qian, T. Diminishing interfacial turbulence by colloid-polymer electrolyte to stabilize zinc ion flux for deep-cycling Zn metal batteries. *Adv. Mater.* **2022**, *34*, No. 2200131.
(51) Liu, Y.; et al. Enhancing two-electron reaction contribution in MnO_2 cathode material by structural engineering for stable cycling in aqueous Zn batteries. *ACS Nano* **2023**, *17*, 14792−14799.
(52) Perdew, J. P.; Burke, K.; Ernzerhof, M. Generalized gradient approximation made simple. *Phys. Rev. Lett.* **1996**, *77*, 3865.
(53) Wang, M.; Jiang, L.; Kim, E. J.; Hahn, S. H. Electronic structure and optical properties of $Zn(OH)_2$: LDA+U calculations and intense yellow luminescence. *RSC Adv.* **2015**, *5*, 87496−87503.
(54) Togo, A. First-principles phonon calculations with phonopy and phono3py. *J. Phys. Soc. Jpn.* **2023**, *92*, No. 012001.

https://doi.org/10.1021/acsnano.4c04795
ACS Nano 2025, 19, 3135−3146

(55) Birch, F. Finite elastic strain of cubic crystals. *Phys. Rev.* **1947**, *71*, 809.
(56) Ong, S. P.; et al. Phase stability, electrochemical stability and ionic conductivity of the $Li_{10\pm1}MP_2X_{12}$ (M= Ge, Si, Sn, Al or P, and X= O, S or Se) family of superionic conductors. *Energy Environ. Sci.* **2013**, *6*, 148−156.
(57) Guo, S.; Qin, L.; Hu, C.; Li, L.; Luo, Z.; Fang, G.; Liang, S. Quasi-Solid Electrolyte Design and In Situ Construction of Dual Electrolyte/Electrode Interphases for High-Stability Zinc Metal Battery. *Adv. Energy Mater.* **2022**, *12*, No. 2200730.
(58) Pan, Y.; Liu, Z.; Liu, S.; Qin, L.; Yang, Y.; Zhou, M.; Sun, Y.; Cao, X.; Liang, S.; Fang, G. Quasi-Decoupled Solid−Liquid Hybrid Electrolyte for Highly Reversible Interfacial Reaction in Aqueous Zinc−Manganese Battery. *Adv. Energy Mater.* **2023**, *13*, No. 2203766.
(59) Guan, Q.; et al. In situ construction of organic anion-enriched interface achieves ultra-long life aqueous zinc-ion battery. *Chem. Eng. J.* **2023**, *476*, No. 146534.
(60) Du, H.; Wang, Y.; Kang, Y.; Zhao, Y.; Tian, Y.; Wang, X.; Tan, Y.; Liang, Z.; Wozny, J.; Li, T.; et al. Side Reactions/Changes in Lithium-Ion Batteries:Mechanisms and Strategies for Creating Safer and BetterBatteries. *Adv. Mater.* **2024**, *36*, No. 2401482.
(61) Li, Q.; Chen, A.; Wang, D.; Pei, Z.; Zhi, C.; et al. "Soft Shorts" Hidden in Zinc Metal Anode Research. *Joule* **2022**, *6*, 273−279.
(62) Lin, Y.; et al. Dendrite-free Zn anode enabled by anionic surfactant-induced horizontal growth for highly-stable aqueous Zn-ion pouch cells. *Energy Environ. Sci.* **2023**, *16*, 687−697.
(63) Ge, H.; et al. An ionically cross-linked composite hydrogel electrolyte based on natural biomacromolecules for sustainable zinc-ion batteries. *Nanoscale Horizon* **2024**, *9*, 1514.
(64) Liu, Z.; Li, G.; Xi, M.; Huang, Y.; Li, H.; Jin, H.; Ding, J.; Zhang, S.; Zhang, C.; Guo, Z. Interfacial Engineering of Zn Metal via a Localized Conjugated Layer for Highly Reversible Aqueous Zinc Ion Battery. *Angew. Chem., Int. Ed.* **2024**, *63*, No. e202319091.

https://doi.org/10.1021/acsnano.4c04795
ACS Nano 2025, 19, 3135−3146